

Soft Matter

Accepted Manuscript

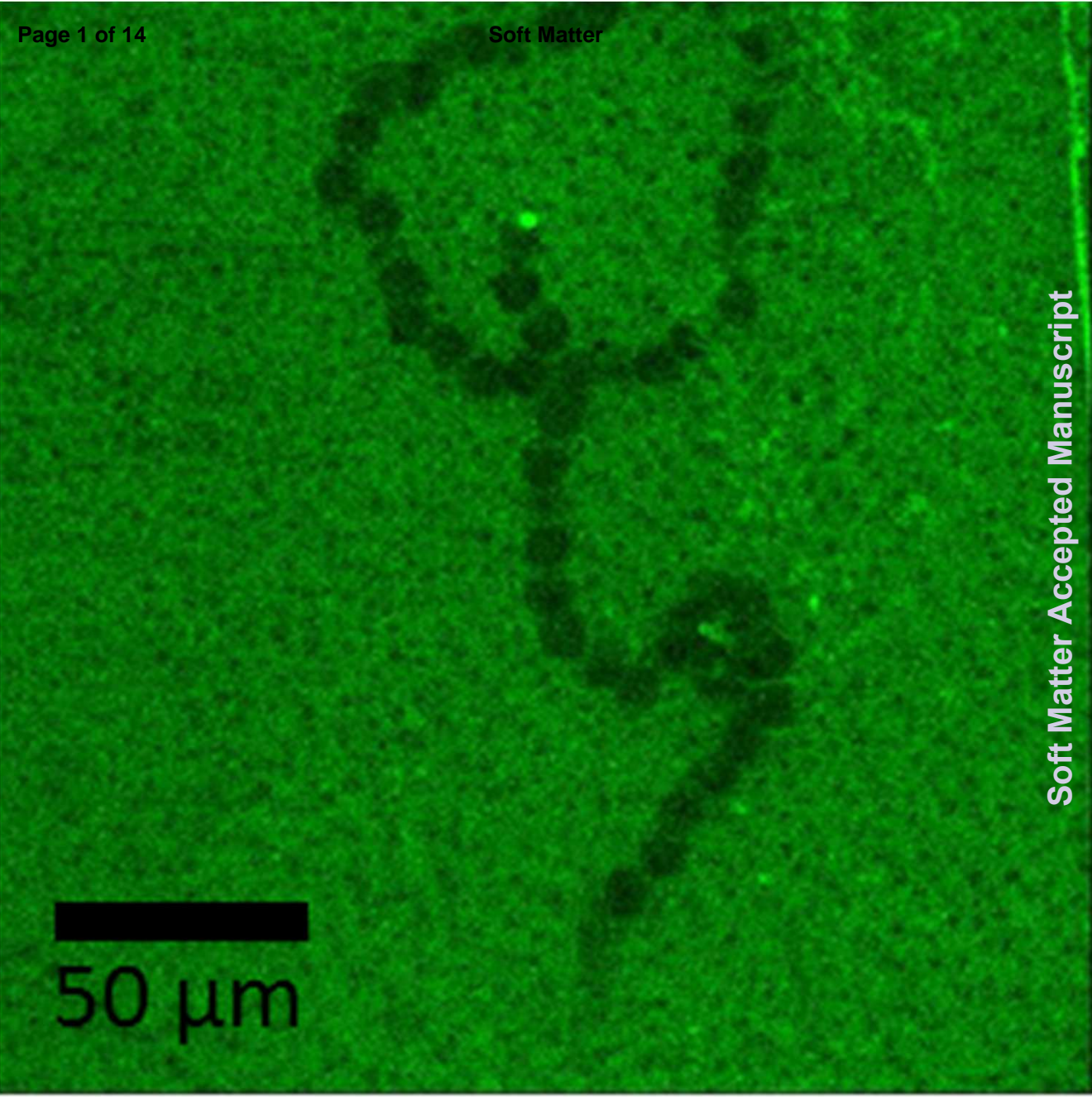


This is an *Accepted Manuscript*, which has been through the Royal Society of Chemistry peer review process and has been accepted for publication.

Accepted Manuscripts are published online shortly after acceptance, before technical editing, formatting and proof reading. Using this free service, authors can make their results available to the community, in citable form, before we publish the edited article. We will replace this *Accepted Manuscript* with the edited and formatted *Advance Article* as soon as it is available.

You can find more information about *Accepted Manuscripts* in the [Information for Authors](#).

Please note that technical editing may introduce minor changes to the text and/or graphics, which may alter content. The journal's standard [Terms & Conditions](#) and the [Ethical guidelines](#) still apply. In no event shall the Royal Society of Chemistry be held responsible for any errors or omissions in this *Accepted Manuscript* or any consequences arising from the use of any information it contains.



50 μm

Jumping acoustic bubbles on lipid bilayers[†]

Christelle Der Loughian,^{a‡} Pauline Muleki Seya,^{b‡} Christophe Pirat,^a Claude Inserra,^b Jean-Christophe Béra,^b and Jean-Paul Rieu^a

Received Xth XXXXXXXXXXXX 20XX, Accepted Xth XXXXXXXXXXXX 20XX

First published on the web Xth XXXXXXXXXXXX 200X

DOI: 10.1039/b000000x

In the context of sonoporation, we use supported lipid bilayers as a model for biological membranes and investigate the interactions between the bilayer and microbubbles induced by ultrasound. Among the various types of damages caused by bubbles on the surface, our experiments exhibit a singular dynamic interaction process where bubbles are jumping on the bilayer, forming a necklace pattern of alteration on the membrane. This phenomenon was explored with different time and space resolutions and, based on our observations, we propose a model for a microbubble subjected to the combined action of Van der Waals, acoustic and hydrodynamic forces. Describing the repeated jumps of the bubble, this model explains the lipid exchanges between bubble and bilayer.

1 Introduction

In the context of intracellular drug delivery for biomedical applications, the transport of bioactive compounds (such as fluorescent markers, siRNA, proteins) with low cytotoxicity and damaging effects remains challenging. Without the use of viral vectors, sonoporation, *i.e.* the permeabilization and poration of the cell membrane by ultrasound technique¹, enables the delivery of various drugs with minimal immunological responses, with the advantage of a noninvasive spatially targeted in-vivo delivery thanks to the possibility of focusing acoustic energy. However, the mechanisms underlying sonoporation-mediated transmembrane and transcellular transport are not well understood, as it implies the inherently nonlinear phenomenon of acoustic cavitation. Acoustic cavitation is the nucleation and growth of submicron-sized gas nuclei, their linear and nonlinear radial oscillations (stable cavitation regime) and eventually their rapid collapse (inertial cavitation regime). According to each of these cavitation regimes, different mechanisms have been proposed to explain the temporarily opening of cell membrane corresponding to reversible sonoporation. The dominant hypothesis are (i) the generation of shear stress on the cell surface resulting from the microbubble-induced microstreaming^{2,3}, (ii) shock pressure waves induced by collapsing bubbles in the inertial cavitation regime^{4,5} and (iii) microjets induced by nonspherical oscillations of a bubble closed to a rigid or soft boundary^{6,7}. With the objective of limiting cell mortality induced by violent bubble collapse, current investigations focused on the stable oscillation of microbubbles nearby rigid⁸ or soft (cells⁹ or lipid bilayers¹⁰) surfaces, and even directly in contact with cells^{11,12}. When stuck to a rigid surface, a stable oscillating bubble can exhibit a translational

motion of its center of mass (Narcissus effect¹³) coupled to its radial oscillations, and surface modes can develop when exposing bubbles to sufficiently high driving pressures¹⁴. When bubbles are oscillating nearby¹⁵ or attached to an individual biological interface¹², the compression and expansion phases of the bubble oscillation lead to pushing and pulling behavior on the cell membrane inducing hydrophilic pores¹⁵ and cell membrane targeted damages with a possibility of repair process^{12,16}. Understanding the bubble-cell interaction is consequently crucial in the optimization of ultrasound-mediated drug internalization. In order to get better insights in bubble-cell interaction, an ultrasound device dedicated to the sonoporation of adherent cells has been designed with the possibility of real-time observation under microscope during sonication, that has demonstrated its efficiency in sonoporating an adherent cell monolayer¹⁷. In this paper we focus on the fundamental interaction of cavitating microbubbles and a supported biomimetic membrane, putting into evidence a new dynamic interactive process where microbubbles jump on the membranes. This particular behavior appears at a first glance similar to the dynamics of bouncing ball¹⁸ or droplets bouncing on a vibrating fluid bath¹⁹, even if the mechanisms underlying the jumping bubble do not imply a vibrating surface. Thus, microscopic visualizations were carried out here to better understand the physics of such oscillating and moving gas bubbles, and a mechanical model is proposed, with a particular care devoted to possible lipid exchange between bubble and

membrane.

2 Materials and Methods

2.1 Membrane preparation

All lipids were purchased from Avanti Polars Lipids. Supported DOPC (dioleoylphosphatidylcholine) or DLPC (dilauroylphosphatidylcholine) bilayers (fluid phases at room temperature) were prepared with 5% of the fluorophore 16:0-12:0 NBD-PC (reference 810131P) and deposited at the bottom glass surface of a culture well (Labtek; Thermo Scientific Nunc; dimensions: 20 x 20 mm², volume: 2 mL) by the vesicle fusion method²⁰ (Figure 1B). Briefly, glass was cleaned with ultra-pure water and soap (microson, Fisher) in an ultrasonic bath twice 20 min at 40°C and extensively rinsed with ultra-pure water after each bath. A 25 mg/ml vesicle solution with 2 mM CaCl₂ was incubated at room temperature during 15 min onto the hydrophilic glass surfaces followed by extensive rinsing^{21,22}. DPPC (dipalmitoylphosphatidylcholine) bilayers shown in Fig. 2 (gel phase at room temperature), containing 1% of NBD-PC, were deposited on hydrophilic slide glass by the Langmuir-Blodgett (LB) deposition method at 45 mN/m surface pressure²³ (Figure 1A).

2.2 Sonoporation setup

The culture well containing the supported bilayer is included in a microscope stage (see Figure 1C) with two plane piezoelectric transducers (Ferroperm PZ 26; resonance frequency 426.5 kHz; dimensions: 18 x 3 mm²) which are facing each other on two opposite sides of this culture well. A flush-mounted needle hydrophone (Onda HNR-0500) located on another side of the well passively listens the inertial cavitation activity in the sonicated medium. The signal supplied to the transducers is a sinusoidal continuous wave which is synthesized within a FPGA system (Field-Programmable Gate Array; PXIe-7965R card; NI) and is provided by the Digital-to-Analog Converter of the FPGA module (16 bits, 100 MHz sampling frequency, NI-5781R module), subsequently amplified by a power amplifier (24 V, 4.8 A, 50 MHz, Kalmus). The hydrophone signal, after amplification (Müller-Voltage Amplifier, +18 dB), is acquired by the Analog-to-Digital Converter device of the FPGA module (14 bits resolution, 100 MHz sampling frequency, NI-5781R module) and the inertial cavitation activity is estimated through a Fast Fourier

Transform. In the whole experiments the acoustic intensities are ranged between [0.7-2.8] W/cm², which correspond to acoustic pressures between [1-2] bars. The acoustic field in the well, mapped at low acoustic intensity ($I_a=0.6$ W/cm²) with an optical fiber hydrophone (Precision acoustic LTD), revealed the presence of a quasi-stationary pressure field corresponding to rectangular cavity mode (8,4,1) in the (x,y,z) coordinate system (see Figure 2). Along the vertical axis e_z , the acoustic field is composed of 1.5 wavelength between the bottom (zero acoustic velocity) and the free water/air interface at the top (zero acoustic pressure)¹⁷.

2.3 Visualization setup

The visualization of the interaction between the cavitation bubbles and the lipid bilayer is done using fluorescence microscopy (Nikon TE2000 inverted microscope). A 480±10 nm bandpass excitation filter enables the observation of the NBD-PC stained lipids. To demonstrate the existence of water inside the jumping bubbles, the water soluble dye Sulforhodamine B (SRB, Sigma) is added in the solution at about 10 µg/ml and is excited at 540 nm. Real-time visualization of the interaction between bubbles and membranes are realized with a 10x PL FL objective (NA 0.3, Nikon), at 30 frames per second using a Neo sCMOS camera (Andor, Dublin). Images with a greater spatial resolution are obtained with a 40x PL FL objective (NA 0.75, Nikon), reducing the acquisition speed to 18 frames per second. Observations were also performed with a confocal microscope (Leica TCS SP5 II), allowing to observe simultaneously the sample in fluorescence (488 nm excitation) and in transmission.

3 Results and discussion

3.1 Interactions of cavitating bubbles with membranes: a quasi-static view.

We first present an experiment at relatively low spatial and temporal resolution (10x objective and 5 sec/image) in order to describe the severe effects, especially at large scales, of cavitating bubbles on a supported biomimetic membrane. This membrane is a DPPC bilayer deposited by the LB deposition method on a glass slide which was transferred under water at the bottom of the culture well. When applying ultrasound, a bubble cloud appears in transmission images (Fig. 2A'-B') but also in fluorescence (Fig. 2A-B, and see also supporting movie M1). As there are no (or very few) lipids in the liquid medium, the fact that bubbles are visible in fluorescence indicates that they collected fluorescent lipids from the bilayer. Dark circular impacts are observed on the lipid bilayer at the same location from which a given bubble moved away, revealing lipid detachment from the bilayer. A bilayer location that has been

^a Institut Lumière Matière, UMR5306 Université Lyon 1-CNRS, Université de Lyon 69622 Villeurbanne cedex, France; E-mail: jean-paul.rieu@univ-lyon1.fr

^b Inserm, U1032, Lyon, F-69003, France; Université de Lyon, Lyon, F-69003, France.

‡ These authors contributed equally to this work.

covered by a bubble cloud is almost free of lipids once the cloud moved away (see arrowheads in Fig. 2A-B). This confirms that cavitation bubbles interact strongly at the bottom of the well with the lipid bilayer. These interactions are spatially located at both nodal and antinodal positions of the acoustic pressure field at the bottom of the well, according to the linear Bjerknes force theory²⁴. Indeed, an oscillating bubble is subjected to a radiation force (primary Bjerknes force) that pushes it towards particular locations depending on its radius compared to the resonant one ($R_{res} = 7 \mu\text{m}$ in our frequency conditions according to the Minnaert theory²⁵). Bubbles whose radii lie below (respectively above) the resonant size would move toward the antinodal (respectively nodal) location of the acoustic pressure field. When considering a sufficiently strong acoustic field, the coupling between translational motion and radial oscillations of the bubble could lead to the inversion of the linearly stable and unstable equilibrium location²⁶. This could explain the presence of both small and large bubbles at the same location (as observed in Figure 2).

Inside the bubble cloud, the larger bubbles of radius $R_b \geq 25 \mu\text{m}$ may remain at the very same position during a few minutes (see arrows in Fig. 2A-B). The fluorescence under these large stationary bubbles is slightly larger than the fluorescence level of the intact bilayer (*i.e.*, about 1.5-fold, see below a more precise quantification at larger magnification). On the other hand the small bubbles are frequently lost from one image to the next, due to their higher mobility. But, permanent damages in the lipid bilayer can be used as a memory marker of their trajectory. In the top part of the figure, far from the main bubble cloud location, cracks appear on the membrane. These cracks could result from the transitory passing in this zone of fast microbubbles not easily visible at such a low temporal resolution. Once ultrasound was stopped, we examined at a larger magnification this area and found interesting bubble trajectories that resemble "a pearl necklace" (Fig. 2C). Indeed, it appears that a given bubble caused circular holes of about 10-15 μm diameter in the bilayer, and apparently jumped by a distance close to its diameter to produce new holes. The necklace like trajectories of these jumping bubbles appear random at long times. In regions far from the acoustic pressure nodes and antinodes, bubbles are not observed, nor are particular bilayer damages.

In the following, we directly deposited lipid bilayers at the bottom of the culture well in order to avoid unwanted motion of the glass slide with ultrasound. To achieve it, we used the vesicle fusion method. In addition to the possibility of forming bilayers at the bottom of wells, this deposition method enables the rejuvenation of samples degraded by the cavitating bubbles. We used lipids in the fluid phase (DOPC or DLPC) at room temperature to avoid vesicle incubation at high temperature (above the melting temperature of lipid membranes) but we mostly obtained the same qualitative degradation map

after applying ultrasound with DPPC (gel phase, Fig. 2).

3.2 Jumping bubble dynamics.

By recording the vicinity of the bubble cloud with an epifluorescence microscope equipped with a fast sensitive camera, we could observe the very fascinating behavior of jumping bubbles (see Fig. 3A and supplementary movie M2 recorded at 30 images/sec, realtime display). When a bubble nucleates and reaches the surface, it starts to collect lipids during about two seconds and suddenly jumps to another position. Once the bubble has jumped, lipids are removed from the surface, leading to a dark disk on the image. Immediately after the jump, the bubble loses most of its fluorescence but it quickly collects lipids again. Interestingly, the intensity tends to saturate just before the jump (Fig. 3B) at about 4 times the intensity of the intact bilayer. The repetition of this cycle (lipid collection, saturation and jump) every 2.3 sec in average leads to the formation of necklace patterns on the bilayer (Fig. 2C).

When observing the jumping bubble dynamics with a greater spatial resolution (see Materials and Methods section for details and supplementary movie M3), the central region under the bubble (ub) appears initially homogeneous with a mean intensity about 1.5 times the one of the intact membrane (im), while the outer edges (oe) are highly fluorescent (up to three times the bilayer level, see Fig. 4A at initial contact time (0 sec) and the corresponding fluorescent profile). We investigated several jumping bubbles and always found this intensity corresponding to three lipid layers under central contacting part at early times (Fig. 5). But as soon as 0.3 sec after the initial contact, several small circular fluorescent structures appear with a fluorescence up to five times the one of the intact membrane (see Fig. 4B at $t = 0.55$ sec and Fig. 5 for the occurrence statistics over several bubbles). These small structures get bigger to finally merge and form one big pocket inside the gas bubble (Fig. 4C). Once the big pocket reaches the external boundary of the bubble, the bubble is detached from the membrane and jumps to another position (just after Fig. 4D). Again, the entire process of internal structure formation and fusion happens within 1 to 3 sec depending on the bubble and is repeated several times. Interestingly, the bubble always lands on a portion of the bilayer yet intact (*i.e.*, not in previously damaged area, see supplementary movie M3).

To investigate the nature of the internal circular structures inside jumping bubbles, the water soluble fluorophore SRB excited at a different wavelength than the fluorescent lipids is added in the water solution (see Materials and Methods section for details and supplementary movie M4). Initially, when the bubble contacts the bilayer (0 sec), it appears dark (Fig. 6) because it prevents the fluorescent solution to be present in the focused area whose thickness is given by the depth of focus of the objective lens (close to 1 μm). But

right after, small fluorescent pockets inside the gas bubble are clearly visible. A coalescence phenomenon of the small pockets into one big drop is observed, followed by the jump of the gas bubble to another position. Hence, these internal structures that contain fluorescent medium (Fig. 6), but also bearing fluorescent lipids at their interface (Fig. 4), are undoubtedly water pockets decorated with lipids under the bilayer (Fig. 7B-C).

3.3 A mechanism for jumping bubbles

According to the necklace observations (Figs. 2C,3,4,6), bubbles exhibiting jumping behaviour are ranged below the resonant radius. We then consider a $6\ \mu\text{m}$ radius bubble stuck on the membrane at a pressure antinode location (which is a stable equilibrium location for a bubble under the resonant size). Based on our fluorescence intensity observations, and on the different forces that could act on the bubble, we propose the following scheme of the lipids organization around the gas bubble during the jumping and pumping process (Fig. 7).

(A) When the bubble is contacting the lipid bilayer, lipids immediately decorate the gas/water bubble interface with a lipid monolayer. This lipid-coated bubble is consequently stabilized on the membrane thanks to interfacial forces (Van der Waals (VDW) forces). These forces arise from the fluctuations in the electric dipole moments of molecules which become correlated as the molecules come closer together, giving rise to an attractive force. According to the intensity profile, the contact area between the lipid-coated bubble and the bilayer is compatible with a trilayer structure (1.5 intensity of fluorescence, Figs. 4,5,7A). This structure is stable due to the large contact area which accounts for a large Van der Waals force. The high value of intensity of fluorescence at the edge can be understood as a high concentration of lipids at the neck between the gas bubble and the membrane. Between two macroscopic flat surfaces in contact separated by a distance d_w and with a contact area A , the VDW force is simply $\mathbf{F}_{VDW} = AH/(6\pi d_w^3)\mathbf{e}_z$ where $H \simeq 7.10^{-21}$ J is the Hamaker constant between PC bilayers²⁷ and $d_w \simeq 2.5$ nm is a typical water separation distance between two PC bilayers²⁸. In the case of a bubble stuck on the membrane, the parameter A corresponds to the area of a disc with a radius R_b (in the case of a hemispheric adherence). For a $6\ \mu\text{m}$ bubble radius, $F_{VDW} \sim 10^{-6}$ N. Buoyancy forces for such a bubble are totally negligible (*i.e.*, $F_B \simeq 10^{-12}$ N) and could not lead to bubble detachment.

(B) Under the action of the acoustic field, the bubble exhibits radial oscillations, resulting in a dynamic bilayer/water/gas contact line leading to the excitation of bubble surface modes^{14,29,30}. The spherical and non-spherical radial oscillations of the bubble, coupled to the possible inhomogeneous adherence, could be responsible for the water infiltra-

tion under the bubble (along the moving contact line for example). Small water pockets are thus created under the bubble (Fig. 7B).

(C) The water drops merge and form a large flat puddle. The presence of this water separates the supported bilayer from the gas/water monolayer at a distance far from the range of VDW forces. Only a small ring of monolayer stays in contact with the bilayer at the periphery of the bubble (Fig. 7C). In this case the contact area A between the bubble and the bilayer decreases and is closed to a peripheral ring. The evolution of VDW force according to the width of the ring in contact (depending on the contact area parameter A) is plotted in Figure 8A. By considering that the ring width is around $0.1\ \mu\text{m}$, $F_{VDW} \sim 10^{-8}$ N.

(D) To detach the bubble, a lift force resulting from the flow near the bottom of the well is taken into account to counterbalance the VDW force. This force is written as $\mathbf{F}_L = C_L \rho_w V_b (\mathbf{U}_w - \mathbf{U}_b) \wedge \nabla \wedge \mathbf{U}_w$, where C_L is a constant around 0.65 in our conditions³¹ and \mathbf{U}_w et \mathbf{U}_b are respectively water and bubble velocity. The bubble is motionless, $\mathbf{U}_b = \mathbf{0}$. The flow considered here is a classical parabolic velocity profile (Poiseuille flow). In the vicinity of the bottom of the well ($z \rightarrow 0$), this lift force reduces to $\langle F_L \rangle \sim \alpha z^3$ with α a function of the bubble radius.

The flow velocity has been estimated with a high-speed camera near the bottom of the well in presence of microparticles (radius $5\ \mu\text{m}$). Flow velocities up to 10 cm/s at about $10\ \mu\text{m}$ above the bottom of the well have been measured, leading to $F_L \sim 10^{-8}$ N by extrapolating a parabolic flow to $z = 0$. When taking into account water infiltration under the bubble and the subsequent lost of adherence, this lift force could compete the VDW force and results in the bubble detachment (Figure 8A).

(E) During bubble rising, the primary Bjerknes force (initially equal to zero when the bubble was stuck at the bottom of the well) will act reversely to the rising (pushing the bubble toward the antinode of the acoustic pressure field). The primary Bjerknes force is defined as $\mathbf{F}_{Bj} = \frac{-4}{3}\pi R_b^3 \nabla P_a(x,y,z,t)$. In our case, this force averaged on an acoustic period is $\langle F_{Bj} \rangle_T = -2\pi^2 P_0^2 \sin(\frac{4\pi z}{L}) R_b^3 / (L \rho R_b^2 (\omega_b^2 - \omega^2))$, where P_0 is the acoustic pressure amplitude, $L = 4\text{mm}$ the water height, $\omega_b^2 = 3kP_{stat}/(\rho R_b^2)$ (where k is the polytropic exponent and P_{stat} is the hydrostatic pressure) and $\omega = 2\pi f_{ac}$ the angular frequency with $f_{ac} = 426.5$ kHz. In the vicinity of the bottom of the well ($z \rightarrow 0$), the acoustic radiation force reduces to $\langle F_{Bj} \rangle \sim \beta z$ with β a function (among other) of the acoustic pressure. By introducing the bubble-wall distance $d = z - R_b$ (insert of Figure 8B), the evolution of the primary Bjerknes force acting on a $6\ \mu\text{m}$ bubble is shown in Figure 8B as a function of the distance d and for different acoustic pressures. When superimposing the estimated lift force, the primary Bjerknes force can compete the hydrodynamic force and

counterbalance it at a distance d of 6, 20 or 40 μm above the bottom of the well for acoustic pressures of 0.5, 1.5 or 3 bars respectively. In the proposed scheme, the competition between acoustic and hydrodynamic forces induces an equilibrium location for the bubble at some height from the bottom, stopping bubble rise, but does not explain its descent. It is worth noting that the hydrodynamic flow observed experimentally is a combination of both an acoustic streaming (induced by the ultrasound waves³²) and a local microstreaming (induced by the bubble oscillations¹³). The unstationary behaviour of each involved phenomenon naturally induces the possibility for the acoustic radiation force to temporarily exceed the lift force, implying the bubble descent (Fig. 7E).

High-speed camera movies revealed that the order of magnitude of jump duration is of \sim ms. In order to check if the proposed acoustic force can bring the bubble back to the lipid bilayer during such a time scale, numerical simulations of a bubble subjected to the primary Bjerknes force and a Reynolds drag force (taking into account the wall and avoiding bubble-wall interpenetration, meaning $d \geq 0$) are performed. The Reynolds drag force is written as $\mathbf{F}_R = -6\pi\mu R_b^2 \dot{z}/(z - R_b)\mathbf{e}_z$ where μ is the dynamic viscosity of the liquid, z the distance between the center of the bubble and the wall and \dot{z} the velocity of the bubble³³. The initial height of the bubble is chosen at 20 μm above the bottom of the well (equilibrium location between the lift and primary Bjerknes forces at 1.5 bars (Figure 8B)). The motion of the falling bubble is shown in Figure 8C as a function of time and for different acoustic pressure amplitudes. At typical acoustic pressure amplitudes encountered experimentally, bubbles can reach the bottom of the well in the range [1-100] nm in a millisecond characteristic time. It is worth noting that, when bubble is approaching the bottom wall, both its velocity and distance from the wall tend to zero, leading to a plateau on the simulated time variation of the Reynolds drag force (Figure 8D). In the vicinity of the bottom wall, the order of magnitude of the Reynolds force is $\sim 10^{-9}$ N, that corresponds to a typical VDW force encountered for infinitesimal contact area (Figure 8A). Thus the bubble could naturally stick on the lipid bilayer as the interfacial forces could counterbalance the Reynolds drag force. Moreover, for such small bubble-wall distance, the possible deviation of the bubble radius induced by its nonlinear spherical or non-spherical oscillations¹⁴ could also create contacting bridges between the bubble surface and the lipid bilayer, and consequently bubble sticking. The whole proposed mechanism is successively repeated on the bubble that creates a necklace like jumping bubble trajectory.

4 Conclusions

In this work, we have shown that supported fluorescent lipid bilayers are valuable systems to study the impact of ultrasound

and cavitating bubbles on surfaces as they keep in memory most of the resulting damages. While studying these damage maps, we incidentally discovered the fascinating necklace trajectories of jumping bubbles. By watching more carefully their dynamics, we found these cavitating bubbles are regularly pumping lipids, allowing the entrance of water and finally jumping to a nearby position with a noticeable regularity. Qualitatively this instability results from a competition between downward oriented van der Waals and Bjerknes forces on one hand and upward oriented hydrodynamic lift forces on the other hand. A main point is that bubbles intensively exchange lipids with the membrane, pumping and providing along their jumping cycle. Microbubbles are used commonly as intravascular ultrasound imaging probes and are becoming increasingly popular tools for targeted drug delivery as they can be loaded with various active molecules, such as antibodies, peptides, and polysaccharides³⁴. Acoustic radiation forces can be used to displace toward and concentrate these objects on vessel walls. However, a better understanding of the interactions between drug loaded microbubbles and cell membranes are a prerequisite for drug delivery in particular for lipophilic and poorly water soluble drugs³⁵. The phenomenon of jumping bubbles may greatly enhance the efficiency of drug delivery by multiplying the period of intimate interaction between bubbles and membranes.

5 Acknowledgments

This work was supported by the French National Research Agency ANR project "SonInCaRe" (2010-TECS-003-01). It was performed within the framework of the LabEx CeLyA (ANR-10-LABX-0060) of Université de Lyon, within the program "Investissements d'Avenir" (ANR-11-IDEX-0007) operated by the French National Research Agency (ANR). We thank Mr E. Evans for fruitful discussions.

References

- 1 M. W. Miller, D. L. Miller and A. A. Brayman, *Ultrasound Med. Biol.*, 1996, **22**, 1131–1154.
- 2 A. A. Doinikov and A. Bouakaz, *J. Acoust. Soc. Am.*, 2010, **128**, 11–19.
- 3 M. M. Forbes, R. Steinberg and W. O'Brien, *Ultrasound Med. Biol.*, 2008, **34**, 2009–2018.
- 4 C. D. Ohl and R. Ikink, *Phys. Rev. Lett.*, 2003, **90**, 214502.
- 5 M. Lokhandwalla, J. A. McAteer, J. C. Williams and B. Sturtevant, *Phys. Med. Biol.*, 2001, **46**, 1245–1264.
- 6 C.-D. Ohl, M. Arora, R. Ikink, N. de Jong, M. Versluis, M. Delius and D. Lohse, *Biophys. J.*, 2006, **91**, 4285–4295.
- 7 P. Prentice, A. Cuschieri, K. Dholakia, M. R. Prausnitz and P. Campbell, *Nature Phys.*, 2005, **1**, 107–110.
- 8 P. Marmottant and S. Hilgenfeldt, *Nature*, 2003, **423**, 153–156.
- 9 P. V. Zinin and J. S. Allen, III, *Phys. Rev. E: Stat., Nonlinear, Soft Matter Phys.*, 2010, **82**, 033901.
- 10 M. S. Malghani, *J. Acoust. Soc. Am.*, 1998, **103**, 1682–1685.

- 11 S. M. Nejad, S. Hosseini, R. Hamid, H. Akiyama and K. Tachibana, *Biochem. Biophys. Res. Commun.*, 2011, **413**, 218–223.
- 12 N. Kudo, K. Okada and K. Yamamoto, *Biophys. J.*, 2009, **96**, 4866–4876.
- 13 P. Marmottant, M. Versluis, N. de Jong, S. Hilgenfeldt and D. Lohse, *Exp. Fluids*, 2006, **41**, 147–153.
- 14 F. Prabowo and C.-D. Ohl, *Ultrason. Sonochem.*, 2011, **18**, 431–435.
- 15 A. van Wamel, K. Kooiman, M. Hartevelde, M. Emmer, F. J. ten Cate, M. Versluis and N. de Jong, *J. Controlled Release*, 2006, **112**, 149–155.
- 16 W. Zhong, W. H. Sit, J. M. F. Wan and A. C. H. Yu, *Ultrasound Med. Biol.*, 2011, **37**, 2149–2159.
- 17 P. Muleki Seya, M. Fouqueray, J. Ngo, A. Poizat, C. Inserra and J.-C. Bera, *accepted in Ultrason Med. Biol.*, 2014.
- 18 J. M. Luck and A. Mehta, *Phys. Rev. E: Stat., Nonlinear, Soft Matter Phys.*, 1993, **48**, 3988–3997.
- 19 Y. Couder, S. Protiere, E. Fort and A. Boudaoud, *Nature*, 2005, **437**, 208.
- 20 A. Brian and H. McConnell, *Proc. Natl. Acad. Sci. USA*, 1984, **81**, 6159–6163.
- 21 L. Tamm and H. McConnell, *Biophys. J.*, 1985, **47**, 105–113.
- 22 S. F. E. Kalb and L. Tamm, *Biochim. Biophys. Acta*, 1992, **1103**, 307–316.
- 23 B. Cross, F. Ronzon, B. Roux and J. Rieu, *Langmuir*, 2005, **21**, 5149–5153.
- 24 A. Eller, *J. Acoust. Soc. Am.*, 1968, **43**, 170–171.
- 25 T. Leighton, *The Acoustic Bubble*, Academic Press, 1994.
- 26 C. Desjoux, P. Labelle, B. Gilles, J.-C. Bera and C. Inserra, *Phys. Rev. E: Stat., Nonlinear, Soft Matter Phys.*, 2013, **88**, 033006.
- 27 D. Leckband and J. Israelachvili, *Q. Rev. Biophys.*, 2001, **34**, 105–267.
- 28 A. Hemmerle, L. Malaquin, T. Charitat, S. Lecuyer, G. Fragneto and J. Daillant, *Proc. Natl. Acad. Sci. U. S. A.*, 2012, **109**, 19938–19942.
- 29 S. ShklyaeV and A. V. Straube, *Phys. Fluids*, 2008, **20**, 052102.
- 30 I. S. Fayzrakhmanova, A. V. Straube and S. ShklyaeV, *Phys. Fluids*, 2011, **23**, 102105.
- 31 D. Legendre, C. Colin and T. Coquard, *Philos. Trans. A Math. Phys. Eng. Sci.*, 2008, **366**, 2233–2248.
- 32 V. Botton, B. Moudjed, D. Henry, H. Ben Hadid, J.-P. Garandet and A. Potherat, Proceedings of the 4th Joint US-European Fluids Engineering Summer Meeting, 2014.
- 33 E. Charlaix, C. Cottin-Bizonne, J. Crassous, S. Leroy, F. Restagno and A. Steinberger, *Reflats de la Physique*, 2011, **22**, 14–18.
- 34 S. R. Sirsi, C. Fung, S. Garg, M. Y. Tianning, P. A. Mountford and M. A. Borden, *Theranostics*, 2013, **3**, 409–419.
- 35 A. Fahr, P. van Hoogevest, S. May, N. Bergstrand and M. Leigh, *Eur. J. Pharm. Sci.*, 2005, **26**, 251–265.

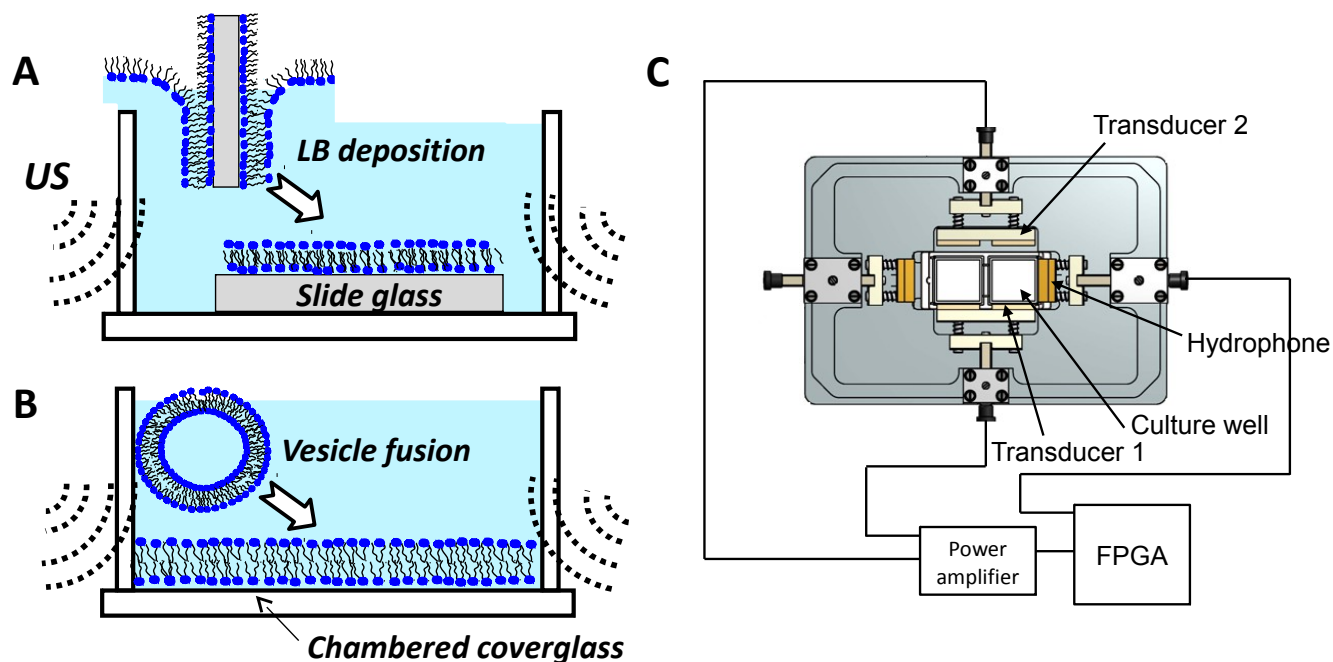


Fig. 1 Schematic representation of the experimental system : A-B) Preparation of supported phospholipids bilayers using Langmuir-Blodgett deposition on slide glass (A), or the vesicle fusion method directly on the bottom of the culture well (chambered coverglass). Ultrasound (US) are applied from the side of the culture well. C) Schematic top view of the sonoporation device : a microscope stage was designed with two piezoelectric transducers and a hydrophone to regulate the cavitation activity in the culture wells.

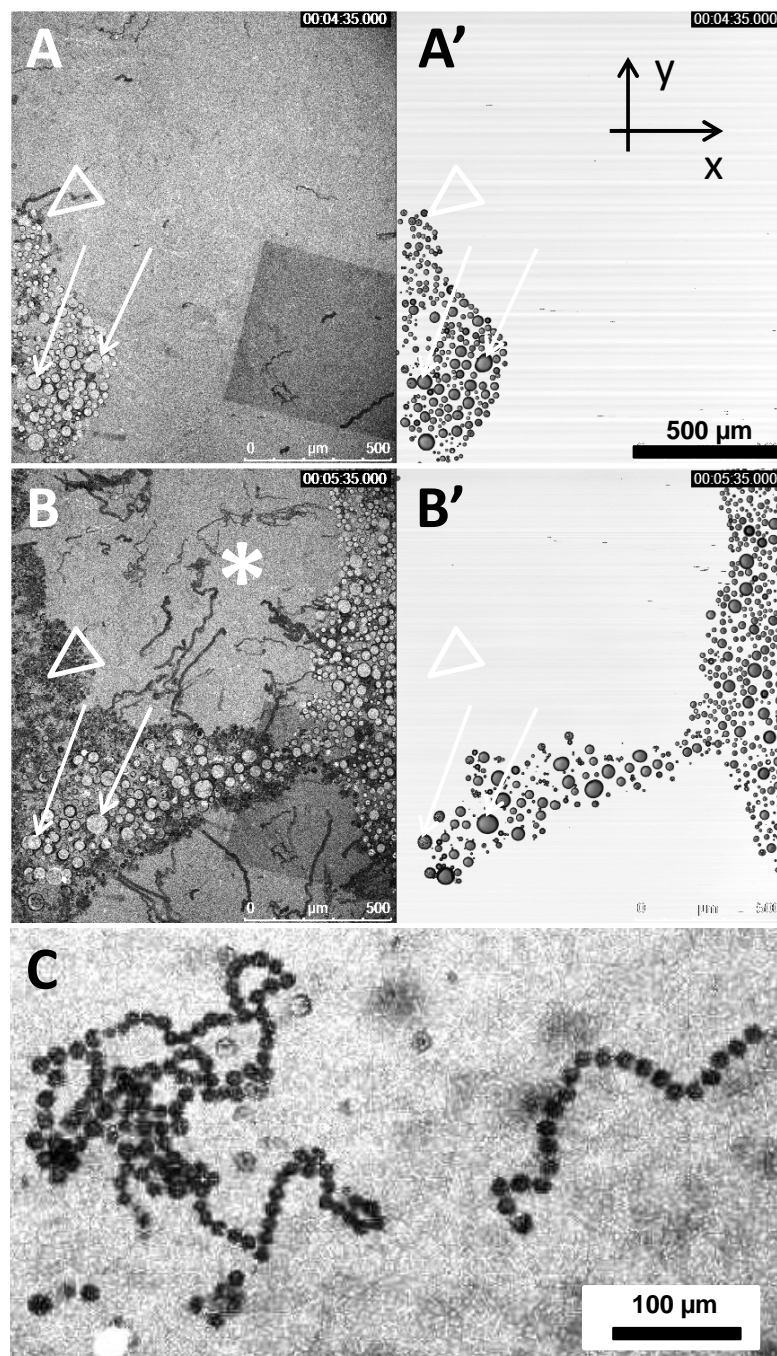


Fig. 2 Confocal microscopy observations of a moving cloud of cavitating bubbles near a glass surface covered by a supported DPPC bilayer with 1% of fluorescent NBD-PC; (A-B) and (C): fluorescence images; (A'-B') right: transmission images. About 4 min after applying ultrasound (A-A'), the cloud appears on the left of the field of view. Bubbles are not only visible in transmission, but also in the fluorescence image, as bubbles collected fluorescent lipids from the supported bilayer and became fluorescent. One min later (B-B'), the cloud moved to the right and strongly degraded the surface that became darker (see arrowheads in A-B). In the bottom right-hand corner, a dark square on the fluorescence image is observed and results from a previous observation of this zone that endured photobleaching. Arrows indicate the positions of two large bubbles that did not move during that time interval. (C) Details at larger magnification of the regions like the one denoted by the asterisk (*) where cracks appeared in (B): the random trajectories of bubbles interacting with the bilayer printed permanent necklace patterns.

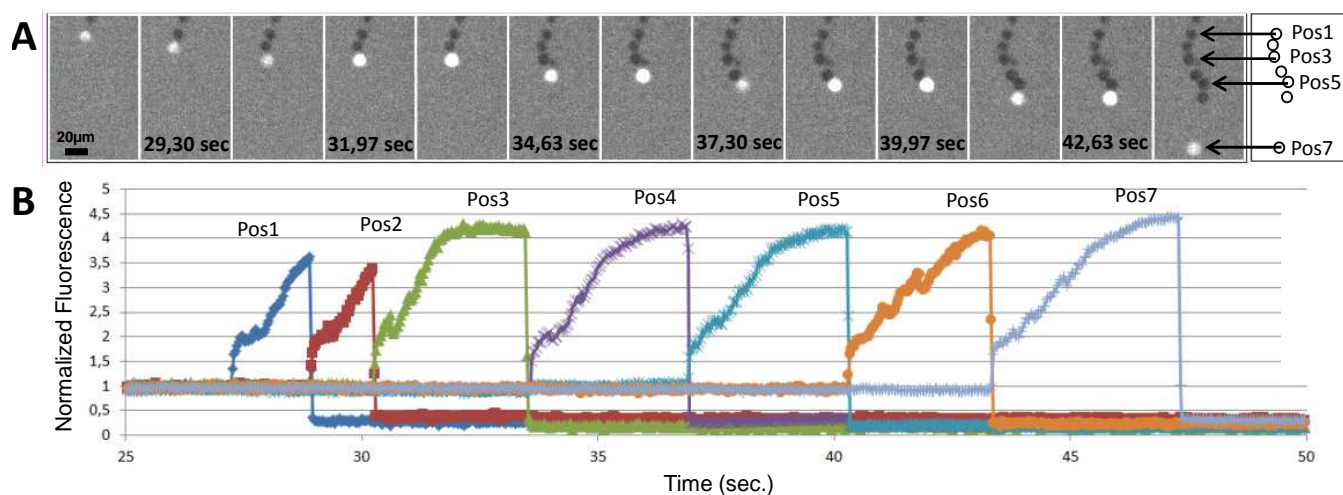


Fig. 3 Fast fluorescence microscopy observations (NBD-PC lipids) of the dynamics of a jumping bubble on a supported DLPC bilayer (30 images/sec). (A) Snapshots every 40 images (1.33 sec): every time the bubble jumps on a new position, it collects fluorescent lipids and becomes brighter; we can notice six jumps and seven different resting positions (right frame); the bubble diameter is approximately constant at $12\mu\text{m}$. (B) Time evolution of the fluorescence mean intensity I in $12\mu\text{m}$ circular areas located at the seven successive resting positions (different colors); the intensity is normalized by the intensity of an intact bilayer after subtracting background; for each position, one can notice three different phases: (i) $I \simeq 1$ before the bubble arrived at that position, (ii) it increases during approximately 2 sec and reaches a maximal value at $I \simeq 4$ and finally (iii) after the jump, I suddenly decreases toward zero as lipids were detached.

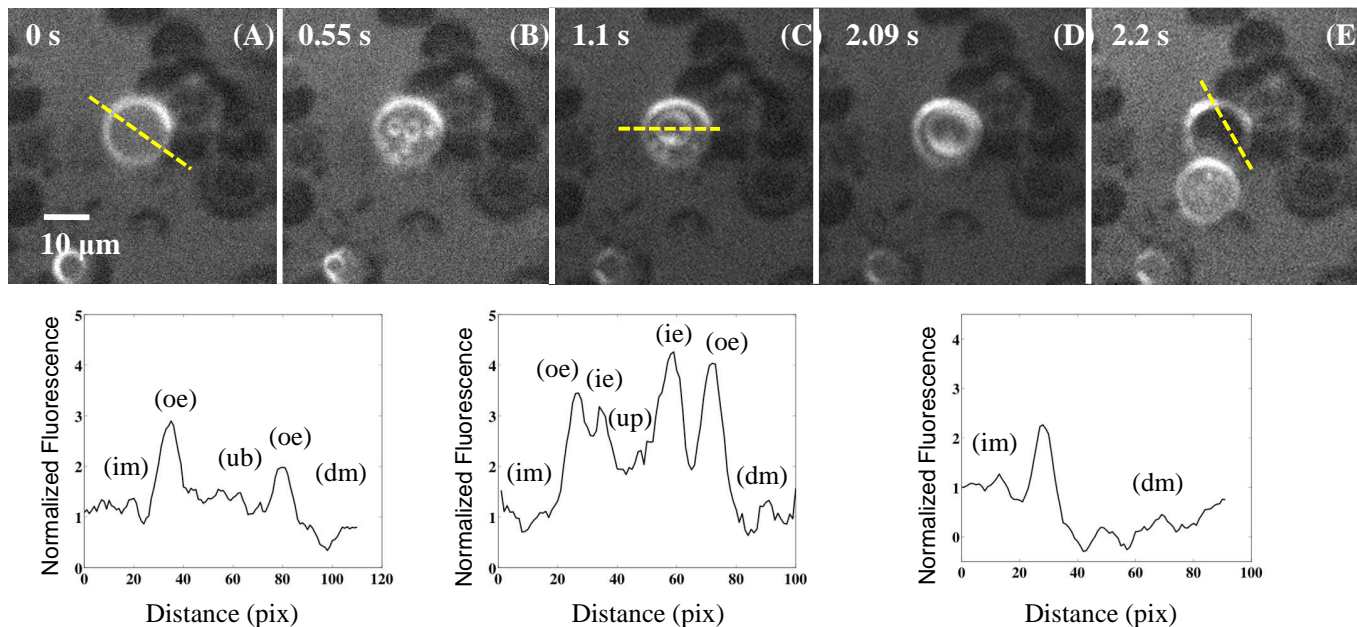


Fig. 4 Fluorescence microscopy observations (NBD-PC lipids) of the dynamics of a jumping bubble on a supported DLPC bilayer at high magnification. The bubble diameter is $12\mu\text{m}$. The normalized fluorescence intensity profiles along the yellow dotted lines depicted in (A,C,E) are displayed under the corresponding images. Four phases can be distinguished : (A) the bubble arrives on the membrane, the bubble is delimited by a fluorescent ring. The intensity profile exhibits different zones : (im) intact membrane outside the bubble, (oe) more fluorescent outer edges, (ub) under the bubble, the intensity of fluorescence is about 1.5 the fluorescence of the intact bilayer, (dm) a damaged membrane zone outside the bubble, due to previous jumps. (B) Small internal structures with fluorescent edges appear inside the gas bubble. (C) These structures merge to form bigger pockets. The intensity profile reveals several zones: (im) intact membrane outside the bubble, (oe) the outer edges as in (A), (ie) inner edges corresponding to the merged small structures inside the bubble, (up) under the pocket, the intensity of fluorescence corresponds to around 2 times the intensity of fluorescence of the intact bilayer, and finally we find outside the bubble the same (dm) damaged membrane as in (A). (D) All the small pockets coalesce into a big pocket and finally the bubble jumps (E). In this last step, we see a zone where the membrane is intact (im) outside the bubble, and a damaged membrane (dm) at the previous position.

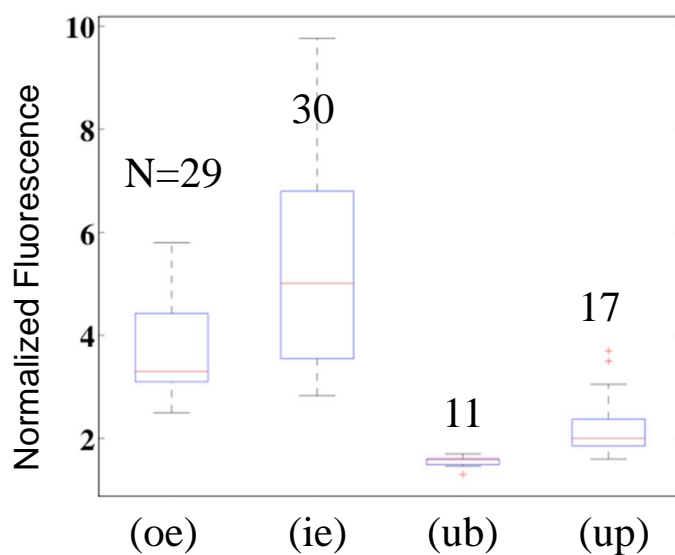


Fig. 5 Boxplot of the mean intensity (from NBD-PC fluorescent lipids) in different regions of the supported membrane: under the bubble (ub), intact membrane far from the cavitating bubbles (im), outer and inner edges of the gas/lipid/water interfaces (oe and ie respectively), under the water pocket (up).

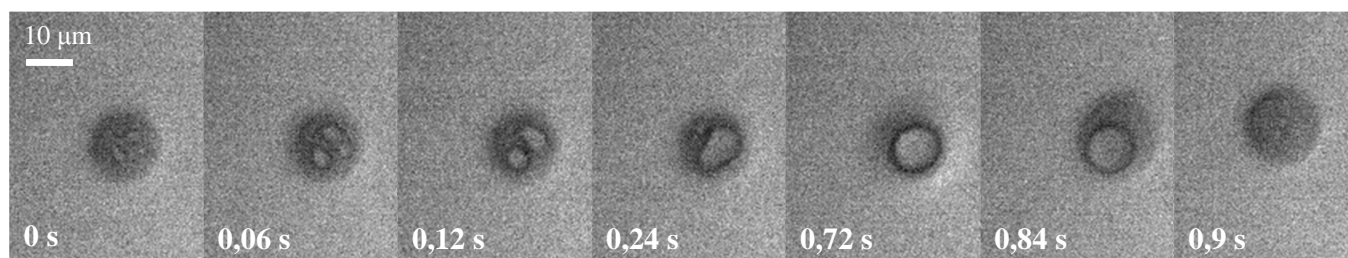


Fig. 6 Fluorescence microscopy observations of the liquid around the jumping bubbles thanks to the soluble dye SRB (high magnification). Initially, the dark halo indicates that gas is present inside the bubble of $14\mu\text{m}$ diameter (A); later, we observe the same typical phases identified in Fig. 4: apparition of small internal fluorescent water structures inside the gas bubble (B-C) that finally merge to form one big water pocket (D-E) before the jump (E).

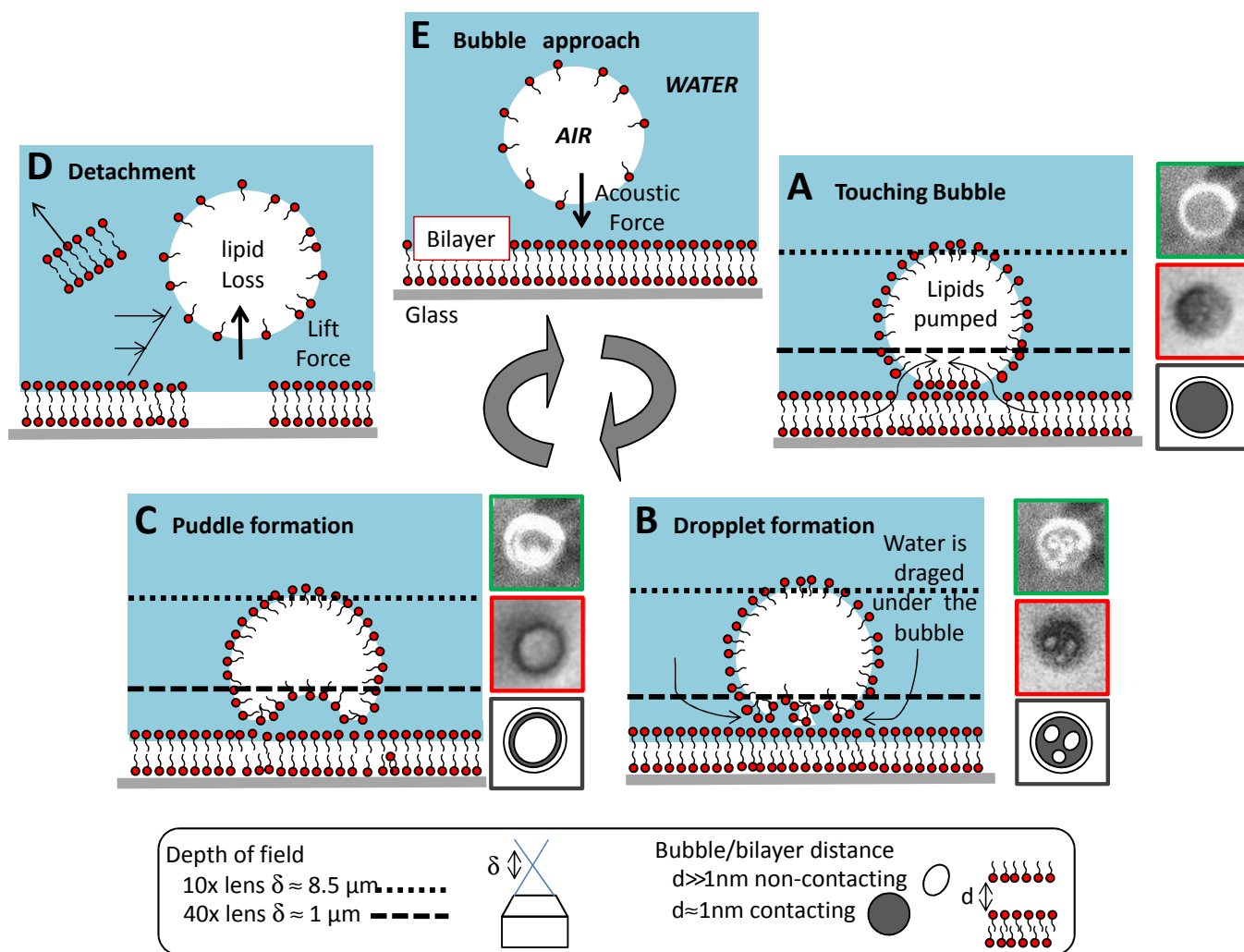


Fig. 7 Proposed mechanism for the jumping process. (A) The bubble touches the membrane, "pumps" lipids and adheres to it thanks to van der Waals forces. (B) The surrounding water enters inside the bubble and forms small drops. (C) The water drops merge to form one big puddle under the gas bubble. (D) The water puddle detaches the gas bubble from the membrane. The bubble is detached when the contact area is too small, preventing the van der Waals force to resist against lift forces. Lipids in the supported membrane under the bubble and decorating water pockets are detached as well from the membranes and pushed again by the radiation force to another position. (E) Due to the radiation force, the gas bubble is pushed close to the membrane. During its jump, the bubble was subjected to lift and horizontal drag forces inducing a slight displacement along the membrane, so that it meets an undamaged bilayer where it adheres again. The dashed lines represent the depth of field for the two used objective lenses. The frames on the right of (A-C) display from top to bottom: a typical fluorescent image of fluorescent lipids, a typical fluorescent image of "fluorescent water", a scheme of the contacting (dark) and non-contacting (light) regions under the bubble.

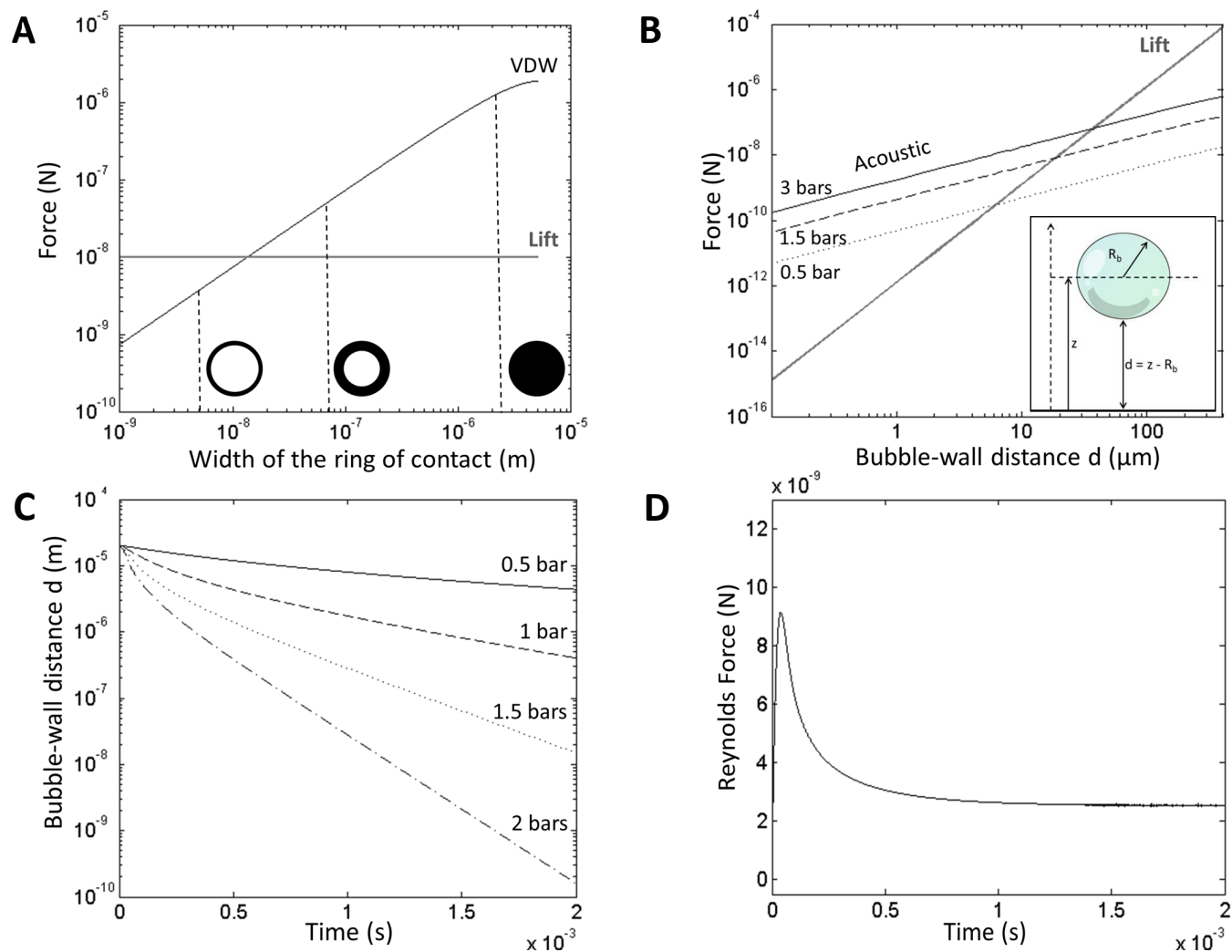


Fig. 8 Estimations of the forces acting on a bubble. (A) Evolution of the VDW force as a function of the width of the ring of contact for a constant outer radius of $6 \mu\text{m}$ compared with an estimation of the lift force at the distance $d = 10 \mu\text{m}$. Three contacting areas A are drawn to represent full, medium and infinitesimal adherence. (B) Evolution of the primary Bjerknes (at 0.5, 1.5 and 3 bars) and lift force (considering a parabolic velocity profile) acting on a bubble as a function of the bubble-wall distance. Inset: schematic view of the bubble-wall distance parameter d for a given bubble of equilibrium radius R_0 . (C) Time evolution of the parameter d for different acoustic pressures for a descending bubble subjected to the primary Bjerknes and Reynolds forces. (D) For the acoustic pressure amplitude 1.5 bars, simulated time variation of the Reynolds drag force acting on the bubble approaching the bottom wall.